Lattice Boltzmann simulations of two-phase flow with high density ratio in axially symmetric geometry

Shiladitya Mukherjee and John Abraham
School of Mechanical Engineering, Purdue University, West Lafayette, Indiana 47907, USA
(Received 1 June 2006; revised manuscript received 19 September 2006; published 5 February 2007)

In this paper, a two-phase lattice Boltzmann (LB) model, developed for simulating fluid flows on a Cartesian grid at high liquid-to-gas density ratios, is adapted to an axisymmetric coordinate system. This is achieved by incorporating additional source terms in the planar evolution equations for the density and pressure distribution functions such that the axisymmetric mass and momentum conservation equations are recovered in the macroscopic limit. Appropriate numerical treatment of the terms is performed to obtain stable computations at high density ratio for this axisymmetric model. The particle collision is modeled by employing multiple relaxation times to attain stability at low viscosity. The model is evaluated by verifying the Laplace-Young relation for a liquid drop, comparing computed frequency of oscillations of an initially ellipsoidal drop with analytical values and comparing the behavior of a spherical drop impinging on a wet wall with prior results. The time evolution of the radial distance of the tip of the corona, formed when the drop impinges, agrees well with prior data.

DOI: 10.1103/PhysRevE.75.026701 PACS number(s): 47.11.−j, 47.61.Jd

I. INTRODUCTION

In recent years, the lattice Boltzmann method (LBM) has emerged as an attractive computational approach for simulating isothermal multiphase fluid flow problems [1–8]. When LBM was introduced, it was based on the phenomenological concept of lattice gas automata [9]. However, later He and Luo [10] showed that the origin of LBM is in the continuous Boltzmann equation and it has a strong theoretical foundation. The LBM is able to simulate complex emergent phenomena from underlying simplified models, and the localized nature of the calculation makes parallelization relatively easy compared to other numerical methods. While LBM has been employed to simulate multiphase flows with promising results, computing high liquid-to-gas density ratios has been a challenging task, until recently, as will be discussed later.

The formal development of LBM is tied with the Cartesian coordinate system. However, many multiphase flow situations exist where computationally expensive full three-dimensional (3D) simulations can be avoided by taking advantage of the inherent axisymmetric nature of the problem. Examples include head-on binary drop collisions and normal impingement of drops on a wall at relatively low Weber numbers. Therefore, it is beneficial to develop LB models for axisymmetric computations. Recently, Premnath and Abraham [11] proposed an index function-based axisymmetric multiple-relaxation-time (MRT) LB model and employed it for the study of binary drop collisions. However, like most other LBM multiphase models, this model becomes numerically unstable at liquid-to-gas density ratios larger than about 10. This instability is due to the presence of large density gradients in the interfacial region. In engineering applications the density ratio is often in the range 50–1000. For example, in diesel engines the injected fuel to compressed oxidizer density ratio is about 50; the density ratio between water and air is 1000 under normal atmospheric conditions. There are recent works addressing this limitation in liquid-to-gas density ratios.

In order to achieve stable computation at high density ratios, Teng *et al.* [12] employed total variation diminishing with artificial compression scheme (TVD/AC). They performed simulations showing phase separation up to a density ratio of 100. Sankaranarayanan *et al.* [13] employed a fully implicit treatment of the Bhatnagar-Gross-Krook (BGK) [14] collision term. They simulated bubble rise with surrounding fluid to a bubble density ratio of about 7. Inamuro *et al.* [15] proposed a free energy-based approach, where the velocity field is first predicted without considering the pressure gradient in the flow field, and then it is corrected by solving a Poisson equation for the pressure field. This scheme requires multiple iterations for the pressure field to converge. They simulated binary drop collisions at a density ratio of 50 and the rise of bubbles in a square duct at density ratios of 50 and 1000. Recently, Lee and Lin [16] presented a pressure-evolution-based high-density ratio LB model in Cartesian coordinate system. They employed this model for the simulation of liquid cylinder impingement on a wet wall when the liquid-to-gas density ratio was 1000 [17]. In an even more recent paper, Zheng *et al.* [18] developed a method which solves a modified lattice Boltzmann equation that had been proposed by Lamura and Succi [19]. They employ their method for test problems involving stationary bubbles and bubbles rising under buoyancy, with a density ratio of 1000.

In this work, the model of Lee and Lin is adapted to an axisymmetric grid. The model is then further modified to employ a multiple-relaxation-time (MRT) [20–22] collision model to enable it to perform stable computations at lower viscosities than possible with the single-relaxation-time BGK model. The approach for developing the axisymmetric model involves the addition of source terms into the transport equations for the distribution functions in the two-dimensional (2D) planar model such that the macroscopic hydrodynamic equations in the axisymmetric framework can be recovered. This approach is similar in spirit to the earlier axisymmetric LB models developed for single-phase flow by Halliday *et al.* [23] and for low density ratio, two-phase flows by Premnath and Abraham. However, developing an axisymmetric model that can perform stable computation at density ratios as high as 1000 involves additional complexity

due to the large density gradient at the interface. Hence, it requires appropriate formulation of the evolution equations for the density and pressure distribution functions and careful numerical treatment of the additional axisymmetric source terms. The model developed in this work is evaluated for three test problems of increasing complexity: Laplace law for static liquid drop, oscillations of an initially ellipsoidal liquid drop, followed by simulation of normal impingement of liquid drop on a wet wall.

This paper is organized as follows. In Sec. II, the axisymmetric high-density ratio LB model is described. For completeness, the essential elements of the high-density ratio 2D planar model of Lee and Lin are also discussed. The numerical implementation of the model is discussed in Sec. III. The model is assessed for accuracy in Sec. IV. The paper closes with a Summary and Conclusion in Sec. V.

II. THE AXISYMMETRIC LB MODEL FORMULATION

A. 2D planar high-density-ratio model

In the high density ratio 2D planar model of Lee and Lin, two distribution functions f and g are employed. The density and fluid property, such as viscosity, are tracked by f, whereas g tracks the pressure and fluid momentum. The macroscopic equations modeled by f are the mass and momentum equations,

$$\partial_t \rho + \partial_k(\rho u_k) = 0 \tag{1}$$

and

$$\rho(\partial_t u_i + u_k \partial_k u_i) = \partial_i(\rho c_s^2 - P) + \partial_j[\mu(\partial_j u_i + \partial_i u_j)] + \kappa\rho\partial_i\nabla^2\rho, \tag{2}$$

respectively. Here, ρ is the density, u the velocity, i the coordinate direction, P the pressure, μ the dynamic viscosity, and κ the surface tension parameter which, in turn, is related to the surface tension σ through the relation

$$\sigma = \kappa \int \left(\frac{\partial \rho}{\partial r}\right)^2 dr, \tag{3}$$

where r is the direction of integration normal to the interface. The corresponding evolution equation for f_α is given by

$$\frac{\partial f_\alpha}{\partial t} + e_{\alpha i}\frac{\partial f_\alpha}{\partial x_i} = -\frac{1}{\lambda}(f_\alpha - f_\alpha^{eq}) + \frac{(e_{\alpha i} - u_i)\left[\partial_i \rho c_s^2 - \rho\partial_i\left(\frac{\partial E_f}{\partial \rho} - \kappa\partial_j^2\rho\right)\right]}{c_s^2}\Gamma_\alpha(\mathbf{u}), \tag{4}$$

where

$$f_\alpha^{eq} = w_\alpha \rho\left[1 + \frac{e_{\alpha i}u_i}{c_s^2} + \frac{(e_{\alpha i}e_{\alpha j} - c_s^2\delta_{ij})u_i u_j}{2c_s^4}\right], \tag{5}$$

$$w_\alpha = \begin{cases} 4/9 & \alpha = 0 \\ 1/9 & \alpha = 1,2,3,4 \\ 1/36 & \alpha = 5,6,7,8 \end{cases}, \tag{6}$$

$$e_\alpha \equiv \begin{cases} (0,0) & \alpha = 0 \\ (\cos\theta_\alpha, \sin\theta_\alpha)c & \theta_\alpha = (\alpha - 1)\pi/2 \quad \alpha = 1,2,3,4, \\ \sqrt{2}(\cos\theta_\alpha, \sin\theta_\alpha)c & \theta_\alpha = (\alpha - 5)\pi/2 + \pi/4 \quad \alpha = 5,6,7,8 \end{cases} \tag{7}$$

$$\Gamma_\alpha(\mathbf{u}) = \frac{f_\alpha^{eq}}{\rho}. \tag{8}$$

Here, α is the discrete particle velocity direction, e the particle velocity, f_α the discrete density distribution function in the α direction, f^{eq} the equilibrium density distribution function, w_α the weight function, λ the relaxation time for the distribution function to reach equilibrium, E_f the excess free energy at the interface over the bulk free energy, c the particle streaming velocity, and c_s the speed of sound. The expression for E_f is obtained from an equation of state (EOS) as follows:

$$E_f(\rho) \approx \beta(\rho - \rho_g^{sat})^2(\rho - \rho_l^{sat})^2, \tag{9}$$

where β is a constant and ρ_g^{sat} and ρ_l^{sat} are densities of gas and liquid phases at saturation, respectively. This EOS results in a density profile given by

$$\rho(z) = \frac{\rho_l^{sat} + \rho_g^{sat}}{2} - \frac{\rho_l^{sat} - \rho_g^{sat}}{2}\tanh\left(\frac{2z}{D}\right), \tag{10}$$

where z is the spatial location normal to the interface and D is the interface thickness. The constants κ and β control D and σ through the relations

$$D = \frac{4}{(\rho_l^{sat} - \rho_g^{sat})}\sqrt{\frac{\kappa}{2\beta}} \tag{11}$$

and

$$\sigma = \frac{(\rho_l^{sat} - \rho_g^{sat})^3}{6}\sqrt{2\kappa\beta}. \tag{12}$$

The pressure distribution function g is related to f by the expression

$$g_\alpha = f_\alpha + \left(\frac{p}{c_s^2} - \rho\right)\Gamma_\alpha(0). \tag{13}$$

This formulation is discussed in prior works [5–7,10,11,17]. The function g is introduced to increase the degree of incompressibility. While fluid phases are tracked by f, the function g maintains the divergence-free condition needed for incompressibility and momentum conservation. The separation of the phase-tracking equation (1) from the momentum balance equation (15) improves the numerical stability of the scheme.

The macroscopic equations modeled by g are

$$\frac{1}{c_s^2}\partial_t p + \partial_k \rho u_k = 0, \tag{14}$$

$$\rho(\partial_t u_i + u_k \partial_k u_i) = \partial_i(\rho c_s^2 - p) + \partial_j[\mu(\partial_j u_i + \partial_i u_j)] + \kappa[\partial_i(\partial_k \rho \partial_k \rho) - \partial_j(\partial_i \rho \partial_j \rho)]. \tag{15}$$

Note that Eq. (14) approaches the zero velocity divergence condition for incompressible flows as $\partial_t p$ approaches zero. Equation (15) is the momentum conservation equation. In the equation, p is the pressure function that varies smoothly across the phase interface and is related to P as

$$p = P - \kappa\rho(\partial_x^2\rho + \partial_y^2\rho) + \frac{\kappa}{2}(\partial_x\rho\partial_x\rho + \partial_y\rho\partial_y\rho). \tag{16}$$

The corresponding evolution equation for g_α is

$$\frac{Dg_\alpha}{Dt} = -\frac{1}{\lambda}(g_\alpha - g_\alpha^{eq}) + \frac{(e_{\alpha i} - u_i)\partial_i(\rho c_s^2 - p)}{c_s^2}[\Gamma_\alpha(\mathbf{u}) - \Gamma_\alpha(0)] + \frac{(e_{\alpha i} - u_i)[\kappa\partial_i(\partial_k\rho\partial_k\rho) - \kappa\partial_j(\partial_i\rho\partial_j\rho)]}{c_s^2}\Gamma_\alpha(\mathbf{u}). \tag{17}$$

B. Axisymmetric high-density-ratio model

We will now discuss the development of the axisymmetric MRT multiphase model. The essential concepts are as follows: The axisymmetric mass and momentum conservation equations can be derived from the 2D planar equations with the addition of source terms in them and the replacement of the planar coordinates with radial and axial coordinates. Two distribution functions are employed: one of them computes density, and the other computes pressure and momentum. The source terms added in the evolution equation for the density distribution function have two purposes. First, they model the mass source term in the continuity equation that arises due to axisymmetry. This can be achieved by adding a source term similar to the one proposed by Premnath and Abraham. Second, a source term is added to account for the axisymmetric contribution of the forcing term required in the evolution equation to maintain the finite thickness of the interface in the high-density-ratio model. The next challenge is to formulate the evolution equation for the pressure distribution function so that stable computations can be performed at a high liquid-to-gas density ratio of 1000. A suitable pressure function is defined such that it varies smoothly across the phase interface and asymptotically reaches the actual pressures in the bulk phases. A similar approach was pursued by Lee and Lin in their development of the high-density-ratio, 2D planar LB model. The form of the pressure function employed in this work, however, involves an additional term due to axisymmetry. The model is then further extended by modifying the evolution equation for the distribution function to model the collision term using MRTs. To maintain a stable scheme at high density ratios the discretization of the axisymmetric source terms and the solution of the discrete density and pressure evolution equations are critical.

The macroscopic equations (1) and (2) can be modified for the axisymmetric framework by transforming them into a cylindrical coordinate system and then setting the azimuthal velocity and azimuthal coordinate derivatives to zero. The resulting equations are

$$\partial_t\rho + \partial_z(\rho u_z) + \partial_r(\rho u_r) = -\frac{\rho u_r}{r}, \tag{18}$$

$$\rho(\partial_t u_z + u_z\partial_z u_z + u_r\partial_r u_z) = \partial_z(\rho c_s^2 - P) + F_{s,z} + \partial_r[\mu(\partial_r u_z + \partial_z u_r)] + F_{ax,z}, \tag{19}$$

$$\rho(\partial_t u_r + u_z\partial_z u_r + u_r\partial_r u_r) = \partial_r(\rho c_s^2 - P) + F_{s,r} + \partial_z[\mu(\partial_z u_r + \partial_r u_z)] + F_{ax,r}, \tag{20}$$

where

$$F_{s,z} = \kappa\rho\partial_z(\partial_z^2\rho + \partial_r^2\rho), \tag{21}$$

$$F_{ax,z} = \frac{\mu}{r}[\partial_r u_z + \partial_z u_r] - \frac{\rho u_r u_z}{r} + \kappa\rho\partial_z\left(\frac{1}{r}\partial_r\rho\right), \tag{22}$$

$$F_{s,r} = \kappa\rho\partial_r(\partial_z^2\rho + \partial_r^2\rho), \tag{23}$$

$$F_{ax,r} = \frac{\mu}{r}[\partial_r u_r + \partial_r u_r] - \frac{\rho u_r u_r}{r} + \kappa\rho\partial_r\left(\frac{1}{r}\partial_r\rho\right). \tag{24}$$

Here, the subscripts r, z denote the radial and axial coordinate directions, respectively. Now, by employing the substitutions

$$(z,r) \rightarrow (x,y), \tag{25}$$

$$(u_z,u_r) \rightarrow (u_x,u_y), \tag{26}$$

in Eqs. (18)–(24) the following set of equations is obtained:

$$\partial_t\rho + \partial_x(\rho u_x) + \partial_y(\rho u_y) = -\frac{\rho u_y}{y}, \tag{27}$$

$$\rho(\partial_t u_x + u_x\partial_x u_x + u_y\partial_y u_x) = \partial_x(\rho c_s^2 - P) + F_{s,x} + \partial_y[\mu(\partial_y u_x + \partial_x u_y)] + F_{ax,x}, \tag{28}$$

$$\rho(\partial_t u_y + u_x\partial_x u_y + u_y\partial_y u_y) = \partial_y(\rho c_s^2 - P) + F_{s,y} + \partial_x[\mu(\partial_x u_y + \partial_y u_x)] + F_{ax,y}, \tag{29}$$

where

$$F_{s,x} = \kappa\rho\partial_x(\partial_x^2\rho + \partial_y^2\rho), \tag{30}$$

$$F_{ax,x} = \frac{\mu}{y}[\partial_y u_x + \partial_x u_y] - \frac{\rho u_y u_x}{y} + \kappa\rho\partial_x\left(\frac{1}{y}\partial_y\rho\right), \tag{31}$$

$$F_{s,y} = \kappa\rho\partial_y(\partial_x^2\rho + \partial_y^2\rho), \tag{32}$$

$$F_{ax,y} = \frac{\mu}{y}[\partial_y u_y + \partial_y u_y] - \frac{\rho u_y u_y}{y} + \kappa\rho\partial_y\left(\frac{1}{y}\partial_y\rho\right). \tag{33}$$

Equations (27)–(33) are similar to Eqs. (1) and (2), written in a 2D Cartesian coordinate system, with the addition of the terms $[-(\rho u_y/y)]$ in the continuity equation and F_{ax} in the momentum equation. The first term in the expression for F_{ax} is proportional to μ and represents the axisymmetric contribution from the viscous stress tensor; the second term is due to inertial force; and the third term, which is proportional to κ, is the axisymmetric contribution from the surface tension. Equations (27)–(29) can be recovered by modifying the evolution equations for f_α in Eq. (4) with the addition of source terms $S_{f\alpha}^{a_0}$ and $S_{f\alpha}^{a_1}$ (see Appendix A for derivation of the equations), i.e.,

$$\frac{\partial f_\alpha}{\partial t} + e_{\alpha i}\frac{\partial f_\alpha}{\partial x_i} = -\frac{1}{\lambda}(f_\alpha - f_\alpha^{eq}) + \frac{(e_{\alpha i} - u_i)\left[\partial_i\rho c_s^2 - \rho\partial_i\left(\frac{\partial E_f}{\partial\rho} - \kappa\partial_j^2\rho\right)\right]}{c_s^2}\Gamma_\alpha(\mathbf{u}) + S_{f\alpha}^{a_0} + S_{f\alpha}^{a_1}, \tag{34}$$

where

$$S_{f\alpha}^{a_0} = -w_\alpha\frac{\rho u_y}{y}, \tag{35}$$

$$S_{f\alpha}^{a_1} = \frac{(e_{\alpha i} - u_i)F_{fi}^{ax}}{c_s^2}\Gamma_\alpha(\mathbf{u}). \tag{36}$$

In Eq. (36),

$$F_{fi}^{ax} = \frac{\rho\nu}{y}[\partial_y u_i + \partial_i u_y] - \frac{\rho u_y u_i}{y} + \kappa\rho\partial_i\left(\frac{1}{y}\partial_y\rho\right). \tag{37}$$

Here, the source term $S_{f\alpha}^{a_0}$ recovers the right side of the continuity equation in Eq. (27) and $S_{f\alpha}^{a_1}$ recovers the axisymmetric momentum source term F_{ax} in Eqs. (28) and (29). Next, the treatment of the distribution function g is discussed.

The set of macroscopic equations (14) and (15) can be modified for the axisymmetric framework as follows:

$$\frac{1}{c_s^2}\partial_t p + \partial_z(\rho u_z) + \partial_r(\rho u_r) = -\frac{\rho u_r}{r}, \tag{38}$$

$$\rho(\partial_t u_z + u_z\partial_z u_z + u_r\partial_r u_z) = \partial_z(\rho c_s^2 - p) + \partial_r[\mu(\partial_r u_z + \partial_z u_r)] + \kappa[\partial_z(\partial_r\rho\partial_r\rho) - \partial_r(\partial_z\rho\partial_r\rho)] + F_{ax,z}, \tag{39}$$

$$\rho(\partial_t u_r + u_z\partial_z u_r + u_r\partial_r u_r) = \partial_r(\rho c_s^2 - p) + \partial_z[\mu(\partial_z u_r + \partial_r u_z)] + \kappa[\partial_r(\partial_z\rho\partial_z\rho) - \partial_z(\partial_r\rho\partial_z\rho)] + F_{ax,r}, \tag{40}$$

where we propose the modified relation between p and P as

$$p = P - \kappa\rho[\partial_z^2\rho + \partial_r^2\rho] + \frac{\kappa}{2}[\partial_z\rho\partial_z\rho + \partial_r\rho\partial_r\rho] - \kappa\frac{\rho\partial_r\rho}{r}. \tag{41}$$

In the axisymmetric computations, p varies smoothly across the phase interface and in the bulk phase $p \equiv P$, since the density gradients are zero. Notice that in the above definition of p, when compared to Eq. (16) in the planar high-density-ratio model of Lee and Lin, a term $-\kappa(\rho\partial_r\rho/r)$ arises due to axisymmetry. This term is proportional to κ/r and therefore accounts for the contribution to p of curvature at the interface in the azimuthal direction. In Eqs. (39) and (40), the terms F_{ax} are given by

$$F_{ax,z} = \frac{\mu}{r}[\partial_r u_z + \partial_z u_r] - \frac{\rho u_r u_z}{r} + \kappa\frac{\partial_r\rho\partial_z\rho}{r}, \tag{42}$$

$$F_{ax,r} = \frac{\mu}{r}[\partial_r u_r + \partial_r u_r] - \frac{\rho u_r u_r}{r} + \kappa\frac{\partial_r\rho\partial_r\rho}{r}. \tag{43}$$

Now, employing the substitution

$$(z,r) \to (x,y), \tag{44}$$

$$(u_z,u_r) \to (u_x,u_y), \tag{45}$$

in Eqs. (38)–(40), the following equations are obtained:

$$\frac{1}{c_s^2}\partial_t p + \partial_x(\rho u_x) + \partial_y(\rho u_y) = -\frac{\rho u_y}{y}, \tag{46}$$

$$\rho(\partial_t u_x + u_x\partial_x u_x + u_y\partial_y u_x) = \partial_x(\rho c_s^2 - p) + \partial_y[\mu(\partial_y u_x + \partial_x u_y)] + \kappa[\partial_x(\partial_y\rho\partial_y\rho) - \partial_y(\partial_x\rho\partial_y\rho)] + F_{ax,x}, \tag{47}$$

$$\rho(\partial_t u_y + u_x\partial_x u_y + u_y\partial_y u_y) = \partial_y(\rho c_s^2 - p) + \partial_x[\mu(\partial_x u_y + \partial_y u_x)] + \kappa[\partial_y(\partial_x\rho\partial_x\rho) - \partial_x(\partial_y\rho\partial_x\rho)] + F_{ax,y}, \quad (48)$$

where

$$F_{ax,x} = \frac{\mu}{y}[\partial_y u_x + \partial_x u_y] - \frac{\rho u_y u_x}{y} - \kappa\frac{\partial_y\rho\partial_x\rho}{y}, \quad (49)$$

$$F_{ax,y} = \frac{\mu}{y}[\partial_y u_y + \partial_y u_y] - \frac{\rho u_y u_y}{y} - \kappa\frac{\partial_y\rho\partial_y\rho}{y}. \quad (50)$$

Equations (46)–(48) are similar to Eqs. (14) and (15) written in the 2D Cartesian coordinate system, with the addition of the terms $[-(\rho u_y/y)]$ in the velocity divergence equation and F_{ax} in the momentum equation. In F_{ax} [Eqs. (49) and (50)], the first term that is proportional to μ is the axisymmetric contribution from the viscous stress tensor, the second term is due to inertial force, and the third term which is proportional to κ is the axisymmetric contribution from the surface tension. To recover Eqs. (46)–(48), we propose to modify the evolution equation for g_α in Eq. (17) with the addition of source terms as follows (see Appendix B for derivation of the equations):

$$\frac{Dg_\alpha}{Dt} = -\frac{1}{\lambda}(g_\alpha - g_\alpha^{eq}) + \frac{(e_{\alpha i} - u_i)\partial_i(\rho c_s^2 - p)}{c_s^2}[\Gamma_\alpha(\mathbf{u}) - \Gamma_\alpha(0)] + \frac{(e_{\alpha i} - u_i)[\kappa\partial_i(\partial_k\rho\partial_k\rho) - \kappa\partial_j(\partial_i\rho\partial_j\rho)]}{c_s^2}\Gamma_\alpha(\mathbf{u}) + S_{g\alpha}^{a_0} + S_{g\alpha}^{a_1}, \quad (51)$$

where

$$S_{g\alpha}^{a_0} = -w_\alpha\frac{\rho u_y}{y}, \quad (52)$$

$$S_{g\alpha}^{a_1} = \frac{(e_{\alpha i} - u_i)F_{gi}^{ax}}{c_s^2}\Gamma_\alpha(\mathbf{u}). \quad (53)$$

In Eq. (53),

$$F_{gi}^{ax} = \frac{\rho\nu}{y}[\partial_y u_i + \partial_i u_y] - \frac{\rho u_y u_i}{y} - \kappa\frac{\partial_i\rho\partial_y\rho}{y}. \quad (54)$$

Here, $S_{f\alpha}^{a_0}$ recovers $-(\rho u_y/y)$ in Eq. (46) and F_{gi}^{ax} recovers $F_{ax,x}$ and $F_{ax,y}$ in Eqs. (47) and (48), respectively.

In the axisymmetric model, density is the order parameter that tracks the interface. This is the same approach adopted by Lee and Lin [17]. As in other two-phase LB approaches [5,10,15,17], the Cahn-Hilliard equation is not solved explicitly. However, by performing a Chapmann-Enskog expansion on the LB equations, a Cahn-Hilliard-like macroscopic equation

$$\partial_t\rho + \partial_i(\rho u_i) = -\frac{\rho u_y}{y} + \partial_j\left[\frac{\nu}{c_s^2}(\partial_j P - \partial_j p)\right] \quad (55)$$

for order parameter can be recovered (see Appendix C for derivation of the equation). In Eq. (55), $-(\rho u_y/y)$ is the axisymmetric source term. Diffusion at the interface is driven by the difference in thermodynamic pressure P and the pressure function p.

The evolution equations, Eqs. (34) and (51), have the single-relaxation-time collision model. We modify them to include a multiple-relaxation-time collision model as follows:

$$\frac{\partial f_\alpha}{\partial t} + e_{\alpha i}\frac{\partial f_\alpha}{\partial x_i} = -\Lambda_{\alpha\beta}(f_\beta - f_\beta^{eq}) + \frac{(e_{\alpha i} - u_i)\left[\partial_i\rho c_s^2 - \rho\partial_i\left(\frac{\partial E_f}{\partial\rho} - \kappa\partial_j^2\rho\right)\right]}{c_s^2}\Gamma_\alpha(\mathbf{u}) + S_{f\alpha}^{a_0} + S_{f\alpha}^{a_1}, \quad (56)$$

and

$$\frac{Dg_\alpha}{Dt} = -\Lambda_{\alpha\beta}(g_\beta - g_\beta^{eq}) + \frac{(e_{\alpha i} - u_i)\partial_i(\rho c_s^2 - p)}{c_s^2}[\Gamma_\alpha(\mathbf{u}) - \Gamma_\alpha(0)] + \frac{(e_{\alpha i} - u_i)[\kappa\partial_i(\partial_k\rho\partial_k\rho) - \kappa\partial_j(\partial_i\rho\partial_j\rho)]}{c_s^2}\Gamma_\alpha(\mathbf{u}) + S_{g\alpha}^{a_0} + S_{g\alpha}^{a_1}. \quad (57)$$

Here, Λ is a generalized collision matrix. References [20–22] may be consulted for the form of this matrix. In this work, we have used, without modification, the formulation including the form of Λ employed in Ref. [22]. Since this is discussed in the literature, details are not included in this paper.

III. NUMERICAL IMPLEMENTATION

In the numerical implementation of this model, the discrete evolution equations are solved in velocity space. For time integration of the collision term along the characteristics, Lee and Lin employed a semi-implicit treatment in their high-density-ratio model, whereas Sankaranarayanan *et al.* employed a fully implicit treatment. However, we employ an explicit treatment of the collision terms. Note that explicit treatment of collision terms has been employed earlier in low-density-ratio LB models. The choice of this discretization is to satisfy the stability condition of the MRT collision model employed in this work. The two-phase and the axisymmetric source terms are discretized by employing the Crank-Nicolson scheme. The discrete evolution equations for f and g may be formulated as

$$f_\alpha(x+e_\alpha\delta_t,t+\delta_t)-f_\alpha(x,t)=-\Lambda_{\alpha\beta}(f_\beta-f_\beta^{eq})|_{(x,t)}+\frac{\delta_t}{2}\frac{(e_{\alpha i}-u_i)\left[\partial_i\rho c_s^2-\rho\partial_i\left(\frac{\partial E_f}{\partial\rho}-\kappa\partial_j^2\rho\right)\right]}{c_s^2}\Gamma_\alpha(\mathbf{u})\Bigg|_{(x,t)}$$
$$+\frac{\delta_t}{2}\frac{(e_{\alpha i}-u_i)\left[\partial_i\rho c_s^2-\rho\partial_i\left(\frac{\partial E_f}{\partial\rho}-\kappa\partial_j^2\rho\right)\right]}{c_s^2}\Gamma_\alpha(\mathbf{u})\Bigg|_{(x+e_\alpha\delta_t,t+\delta_t)}$$
$$+\frac{\delta_t}{2}(S_{f\alpha}^{a_0}+S_{f\alpha}^{a_1})\Bigg|_{(x,t)}+\frac{\delta_t}{2}(S_{f\alpha}^{a_0}+S_{f\alpha}^{a_1})\Bigg|_{(x+e_\alpha\delta_t,t+\delta_t)}, \tag{58}$$

and

$$g_\alpha(x+e_\alpha\delta_t,t+\delta_t)-g_\alpha(x,t)=-\Lambda_{\alpha\beta}(g_\beta-g_\beta^{eq})|_{(x,t)}+\frac{\delta_t}{2}\frac{(e_{\alpha i}-u_i)\partial_i\rho c_s^2}{c_s^2}[\Gamma_\alpha(u)-\Gamma_\alpha(0)]\Bigg|_{(x,t)}+\frac{\delta_t}{2}\frac{(e_{\alpha i}-u_i)\partial_i\rho c_s^2}{c_s^2}[\Gamma_\alpha(u)$$
$$-\Gamma_\alpha(0)]\Bigg|_{(x+e_\alpha\delta_t,t+\delta_t)}+\frac{\delta_t}{2}\frac{(e_{\alpha i}-u_i)[\kappa\partial_i(\partial_k\rho\partial_k\rho)-\kappa\partial_j(\partial_i\rho\partial_j\rho)]}{c_s^2}\Gamma_\alpha(u)\Bigg|_{(x,t)}$$
$$+\frac{\delta_t}{2}\frac{(e_{\alpha i}-u_i)[\kappa\partial_i(\partial_k\rho\partial_k\rho)-\kappa\partial_j(\partial_i\rho\partial_j\rho)]}{c_s^2}\Gamma_\alpha(u)\Bigg|_{(x+e_\alpha\delta_t,t+\delta_t)}$$
$$+\frac{\delta_t}{2}(S_{g\alpha}^{a_0}+S_{g\alpha}^{a_1})\Bigg|_{(x,t)}+\frac{\delta_t}{2}(S_{g\alpha}^{a_0}+S_{g\alpha}^{a_1})\Bigg|_{(x+e_\alpha\delta_t,t+\delta_t)}. \tag{59}$$

Notice that compared to the high-density-ratio model of Lee and Lin, the above equations include source terms to model axisymmetry. Collision terms are treated explicitly instead of with Crank-Nicolson, as in Ref. [17]. Also, in the above formulation, $\Lambda_{\alpha\beta}$ is the generalized collision matrix instead of the single relaxation time of Ref. [17]. The discrete equations are solved in three steps similar to the steps of Lee and Lin. The first step is a prestreaming collision step. In this step the collision and source terms at (x,t) are summed as follows:

$$\bar{f}_\alpha(x,t)=f_\alpha(x,t)-\Lambda_{\alpha\beta}(f_\beta-f_\beta^{eq})|_{(x,t)}$$
$$+\frac{\delta_t}{2}\frac{(e_{\alpha i}-u_i)\left[\partial_i\rho c_s^2-\rho\partial_i\left(\frac{\partial E_f}{\partial\rho}-\kappa\partial_j^2\rho\right)\right]}{c_s^2}\Gamma_\alpha(u)\Bigg|_{(x,t)}$$
$$+\frac{\delta_t}{2}(S_{f\alpha}^{a_0}+S_{f\alpha}^{a_1})\Bigg|_{(x,t)}, \tag{60}$$

$$\bar{g}_\alpha(x,t)=g_\alpha(x,t)-\Lambda_{\alpha\beta}(g_\beta-g_\beta^{eq})|_{(x,t)}$$
$$+\frac{\delta_t}{2}\frac{(e_{\alpha i}-u_i)\partial_i(\rho c_s^2-p)}{c_s^2}[\Gamma_\alpha(u)-\Gamma_\alpha(0)]\Bigg|_{(x,t)}$$
$$+\frac{\delta_t}{2}\frac{(e_{\alpha i}-u_i)[\kappa\partial_i(\partial_k\rho\partial_k\rho)-\kappa\partial_j(\partial_i\rho\partial_j\rho)]}{c_s^2}\Gamma_\alpha(u)\Bigg|_{(x,t)}$$
$$+\frac{\delta_t}{2}(S_{g\alpha}^{a_0}+S_{g\alpha}^{a_1})\Bigg|_{(x,t)}. \tag{61}$$

In the streaming step which follows prestreaming, the collection of terms at (x,t) is streamed into the new location $(x+e_\alpha\delta_t)$ as follows:

$$\bar{f}_\alpha(x+e_\alpha\delta_t,t+\delta_t)=\bar{f}_\alpha(x,t), \tag{62}$$

$$\bar{g}_\alpha(x+e_\alpha\delta_t,t+\delta_t)=\bar{g}_\alpha(x,t). \tag{63}$$

In the poststreaming step, the distribution functions are updated at $(x+e_\alpha\partial_t,t+\partial_t)$ as follows:

$$f_\alpha(x+e_\alpha\delta_t,t+\delta_t)=\bar{f}_\alpha(x+e_\alpha\delta_t,t+\delta_t)+\frac{\delta_t}{2}\frac{(e_{\alpha i}-u_i)\left[\partial_i\rho c_s^2-\rho\partial_i\left(\frac{\partial E_f}{\partial\rho}-\kappa\partial_j^2\rho\right)\right]}{c_s^2}\Gamma_\alpha(u)\Bigg|_{(x+e_\alpha\delta_t,t+\delta_t)}+\frac{\delta_t}{2}(S_{f\alpha}^{a_0}+S_{f\alpha}^{a_1})\Bigg|_{(x+e_\alpha\delta_t,t+\delta_t)}, \tag{64}$$

$$g_\alpha(x+e_\alpha\delta_t,t+\delta_t)=\bar{g}_\alpha(x+e_\alpha\delta_t,t+\delta_t)+\frac{\delta_t}{2}\frac{(e_{\alpha i}-u_i)\partial_i\rho c_s^2}{c_s^2}[\Gamma_\alpha(u)-\Gamma_\alpha(0)]\Big|_{(x+e_\alpha\delta_t,t+\delta_t)}$$
$$+\frac{\delta_t}{2}\frac{(e_{\alpha i}-u_i)[\kappa\partial_i(\partial_k\rho\partial_k\rho)-\kappa\partial_j(\partial_i\rho\partial_j\rho)]}{c_s^2}\Gamma_\alpha(u)\Big|_{(x+e_\alpha\delta_t,t+\delta_t)}+\frac{\delta_t}{2}(S_{g\alpha}^{a_0}+S_{g\alpha}^{a_1})\Big|_{(x+e_\alpha\delta_t,t+\delta_t)}. \quad (65)$$

The density, velocity, and hydrodynamic pressure are computed after the streaming steps in Eqs. (62) and (63) as follows:

$$\rho=\sum_\alpha \bar{f}_\alpha-\frac{\delta_t}{2}\frac{\rho u_y}{y}\Big|_{(x+e_\alpha\delta_t,t+\delta_t)}, \quad (66)$$

$$\rho u_i=\sum_\alpha e_{\alpha\alpha}\bar{g}_\alpha+\frac{\delta_t}{2}\kappa\Bigg[\frac{\partial}{\partial x_i}\left(\frac{\partial\rho}{\partial x_k}\frac{\partial\rho}{\partial x_k}\right)-\frac{\partial}{\partial x_j}\left(\frac{\partial\rho}{\partial x_i}\frac{\partial\rho}{\partial x_j}\right)\Bigg]\Bigg|_{(x+e_\alpha\delta_t,t+\delta_t)}+\frac{\delta_t}{2}\Bigg[\frac{\rho\nu}{y}[\partial_y u_i+\partial_i u_y]-\frac{\rho u_y u_i}{y}-\kappa\frac{\partial_i\rho\partial_y\rho}{y}\Bigg]\Bigg|_{(x+e_\alpha\delta_t,t+\delta_t)}, \quad (67)$$

$$p=c_s^2\sum_\alpha \bar{g}_\alpha+\frac{\delta_t}{2}u_i\frac{\partial\rho c_s^2}{\partial x_i}\Big|_{(x+e_\alpha\delta_t,t+\delta_t)}-c_s^2 w_\alpha\frac{\rho u_y}{y}\Big|_{(x+e_\alpha\delta_t,t+\delta_t)}. \quad (68)$$

In these equations, the terms proportional to $1/y$ are axisymmetric contributions to density, momentum, and pressure. The relaxation parameter $\tau=\lambda/\delta_t$ is linearly interpolated from the density using the relation

$$\tau=\tau_g+\frac{\rho-\rho_g}{\rho_l-\rho_g}(\tau_l-\tau_g), \quad (69)$$

where τ_l and τ_g are relaxation parameters for the liquid and gas, respectively. The relaxation parameter is related to viscosity by [5–7,10,11] $\nu=[\tau-(1/2)]c_s^2\delta_t$. By analogy, the collision matrix $\Lambda_{\alpha\beta}$ at each lattice node is computed by linear interpolation as

$$\Lambda_{\alpha\beta}=\Lambda_{\alpha\beta,g}+\frac{\tau-\tau_g}{\tau_l-\tau_g}(\Lambda_{\alpha\beta,l}-\Lambda_{\alpha\beta,g}), \quad (70)$$

where $\Lambda_{\alpha\beta,l}$ and $\Lambda_{\alpha\beta,g}$ are the collision matrix elements computed using τ_l and τ_g, respectively.

For the stability of the scheme at high density ratios, the use of an appropriate stencil to compute different gradients is critical. The terms $e_{\alpha i}\partial_i\rho$ in Eqs. (34) and (51) and the term $e_{\alpha i}\partial_i[(\partial E_f/\partial\rho)-\kappa\nabla^2\rho]$ in Eq. (34), which arises as a result of the two-phase nature of the flow, are treated as directional derivatives, i.e., the finite differencing of the derivative is performed along the direction of the characteristic $e_{\alpha i}$. The other derivatives in the two-phase source terms are computed as partial derivatives along the coordinate directions. This step is the same as that proposed by Lee and Lin. However, in the axisymmetric model treatment of the axisymmetric source terms are also critical for the stability of the scheme at high density ratios. Therefore, we propose to treat the terms $(\partial_y\rho/y)e_{\alpha i}\partial_i\rho$ in Eq. (51) and $\rho e_{\alpha i}\partial_i[(1/y)\partial_y\rho]$ in Eq. (34), which arise due to axisymmetry, as directional derivatives, while the remaining axisymmetric source terms are treated as partial derivatives. Directional derivatives are computed by employing the following two schemes suggested by Lee and Lin: Second-order central differencing

$$e\delta_t\frac{d\varphi}{dx}\Big|_{(x)}^{2C}=\frac{\varphi(x+e\delta_t)-\varphi(x-e\delta_t)}{2}. \quad (71)$$

Second-order biased differencing

$$e\delta_t\frac{d\varphi}{dx}\Big|_{(x)}^{2B}=\frac{-\varphi(x+2e\delta_t)+4\varphi(x+e\delta_t)-3\varphi(x)}{2}. \quad (72)$$

In the prestreaming collision step the following stencil is used:

$$\frac{d\varphi}{dx}\Big|_{(x)}^{2M}=\frac{d\varphi}{dx}\Big|_{(x)}^{2B},\quad \text{if } \left(\frac{d\varphi}{dx}\right)\Big|_{(x)}^{2B}\times\left(\frac{d\varphi}{dx}\right)\Big|_{(x+e\delta_t)}^{2C}\geqslant 0, \quad (73)$$

$$\frac{d\varphi}{dx}\Big|_{(x)}^{2M}=\frac{d\varphi}{dx}\Big|_{(x)}^{2C},\quad \text{if } \left(\frac{d\varphi}{dx}\right)\Big|_{(x)}^{2B}\times\left(\frac{d\varphi}{dx}\right)\Big|_{(x+e\delta_t)}^{2C}<0. \quad (74)$$

In the poststreaming collision step, the second-order central differencing is employed. The partial derivatives are computed as

$$\frac{\partial\varphi}{\partial x_i}=\sum_{\alpha\neq 0}\frac{w_\alpha e_\alpha\cdot\hat{\mathbf{i}}[\varphi(x+e_\alpha\delta_t)-\varphi(x-e_\alpha\delta_t)]}{2c_s^2\delta_t}, \quad (75)$$

$$\frac{\partial^2\varphi}{\partial x_i\partial x_i}=\sum_{\alpha\neq 0}\frac{w_\alpha[\varphi(x+e_\alpha\delta_t)-2\varphi(x)+\varphi(x-e_\alpha\delta_t)]}{c_s^2\delta_t^2}. \quad (76)$$

IV. RESULTS AND DISCUSSION

The high-density-ratio axisymmetric MRT model developed in the previous section will now be evaluated on some test problems. The dimensional results are presented in lattice units where the velocity is scaled by the particle velocity c and the distance by the lattice spacing δ_x. The first problem

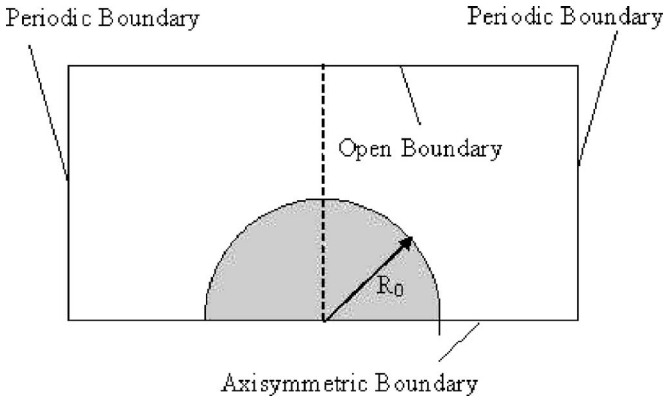

FIG. 1. Schematic of the domain for Laplace law simulation; a spherical drop in equilibrium with the ambient gas.

assesses the ability of the model to reproduce Laplace's law. For a spherical liquid drop in equilibrium with the surrounding fluid, the law states that the pressure p_{in} inside the drop and the pressure p_{out} outside the drop are balanced by the surface tension σ by the following relation

$$\Delta p_{anal} = p_{in} - p_{out} = \frac{2\sigma}{R_0}, \tag{77}$$

where R_0 is the drop radius. The schematic of the simulation setup is shown in Fig. 1. The bottom boundary is the axisymmetric axis. The liquid drop is positioned with its center on the middle of the axisymmetric axis. Periodic boundary conditions are applied on the left and right boundaries, while slip boundary condition is applied to the top. Initially the pressure is set uniform throughout the domain. With time, the pressures inside and outside the drop adjust depending on the value of σ. At equilibrium, the pressure difference between the node at the center of the drop and a node in the ambient is compared with the analytically predicted Δp_{anal} from Eq. (77).

Figure 2 shows a scatter plot of density as a function of radial distance from the drop center at initial condition and in equilibrium. The drop size is $R_0=25$. The domain size is

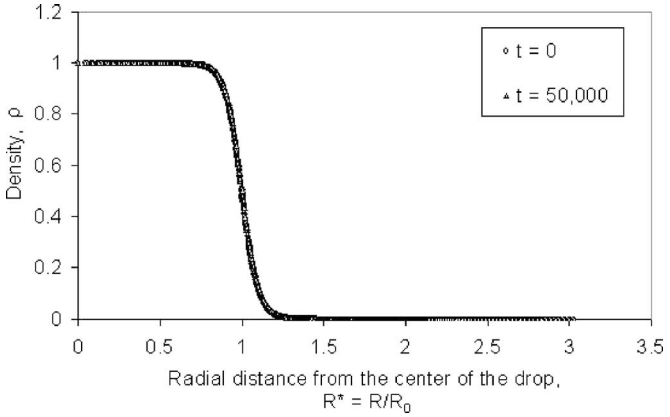

FIG. 2. Scatter plots of initial ($t=0$) and equilibrium ($t=50\,000$) density profiles along the radius of the liquid drop; $D=5$.

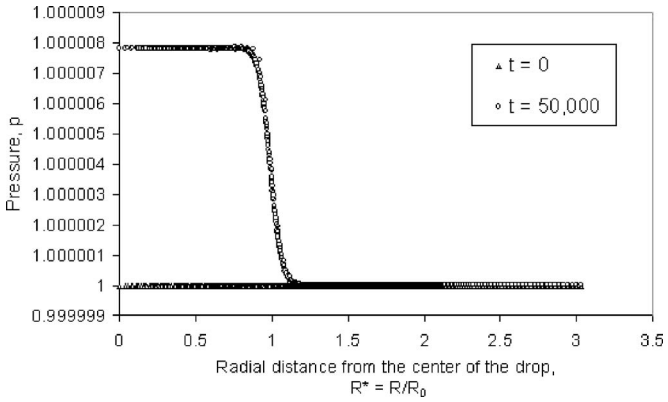

FIG. 3. Scatter plots of initial ($t=0$) and equilibrium ($t=50\,000$) pressure profiles along the radius of the liquid drop; $D=5$.

100×50. The liquid and ambient properties selected are $\rho_l=1.0$, $\rho_l/\rho_g=1000$, $\tau_l=0.505$, $\mu_l/\mu_g=40$, $\sigma=0.0001$, and $D=5$. The equilibrium density profile varies only slightly from the initial density profile, which was set up as a smoothly varying hyperbolic tangent profile formulated in Eq. (10). Therefore mass is conserved with a high level of accuracy, with the mean radius varying less than 1%. The equilibrium density profile also demonstrates a high degree of isotropy, as nearly all points lie on the same curve, irrespective of the direction. In Fig. 3, initial and equilibrium scatter plots of pressure as a function of radial distance from the center is shown. Initially the pressure is uniform throughout the domain at $p=1.0$. At equilibrium, the pressure inside the drop is higher compared to the pressure outside, with a smooth transition in the interfacial region. The computed pressure difference is within 3% of the analytical solution. As D is increased, it is expected that the accuracy of the computed solution will increase and converge toward the analytical solution [Eq. (77)]. This trend is shown in Fig. 4(a), where the percent errors decrease as D is increased. For example, at $D=5$ and 8, percent errors are 2.25% and 0.0125%, respectively. As in other two-phase LB models [1,5,17], spurious velocities are observed at the interfacial region. In Fig. 4(b), the maximum value of the spurious velocity is plotted for two different values of σ, 0.0001 and 0.00 001, while varying D from 3 to 8. The spurious velocity decreases as D is increased and surface tension is lowered.

Next, a dynamical problem is considered, that of liquid drop oscillations. If a liquid drop is slightly perturbed from its equilibrium spherical shape to an ellipsoid, it exhibits oscillatory behavior. Lamb [24] provided the theoretical analysis of this observed phenomenon. The dependence of oscillation frequency on the surface tension of the drop was given as

$$\omega_n^{*2} = n(n-1)(n+2)\frac{\sigma}{\rho_l {R_0}^3}, \tag{78}$$

where ω_n^* is the angular frequency, σ the surface tension, ρ_l the drop density, and R_0 the equilibrium drop radius. The mode of oscillation is denoted by n, which for an initial ellipsoidal shape is 2. In Lamb's work, the effect of liquid

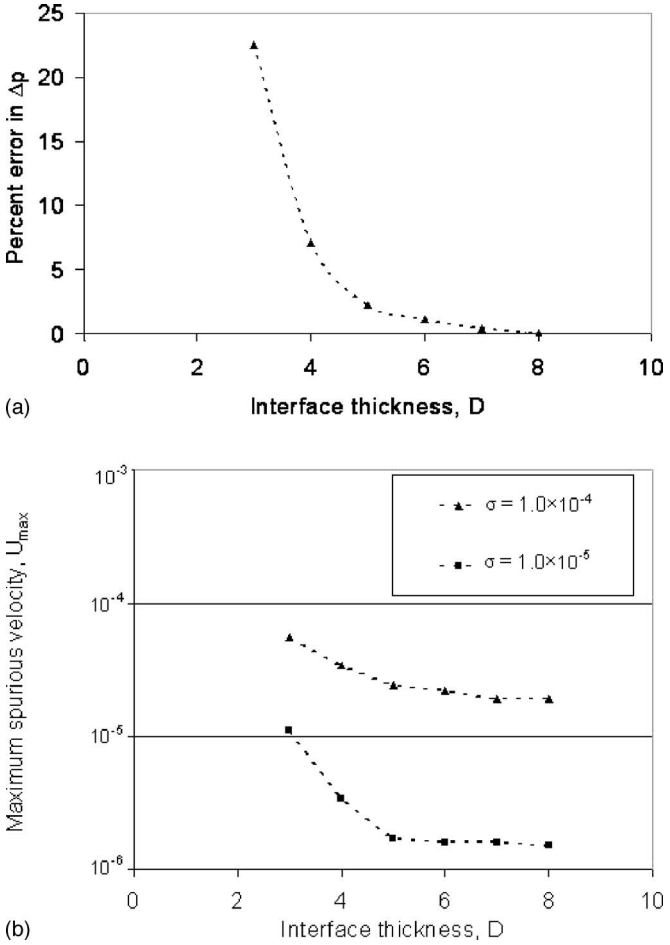

FIG. 4. (a) Differences between analytical and computed pressure differentials for different values of D. (b) Maximum spurious velocity as a function of drop interface thickness D for two values of σ.

viscosity and the surrounding fluid density and viscosity were not considered.

Figure 5 shows the interface oscillations for the drop. The initial configuration of the drop consists of an ellipsoidal shape with minimum radius ($R_{\min}$) and maximum radius

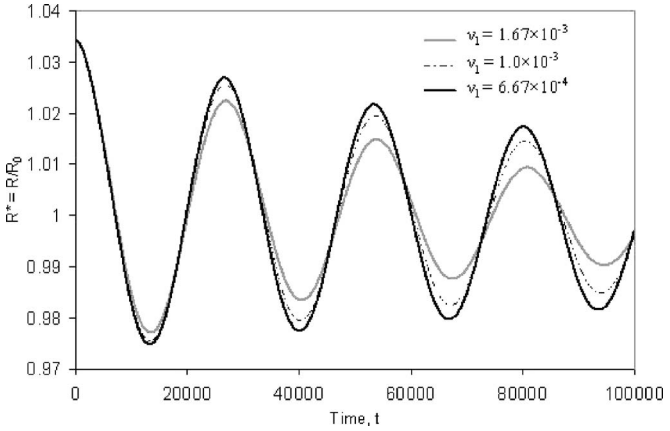

FIG. 5. Oscillation of an initially ellipsoidal drop at different viscosities; $\rho_l/\rho_g=1000$, $\mu_l/\mu_g=40$, and $\sigma=0.0001$.

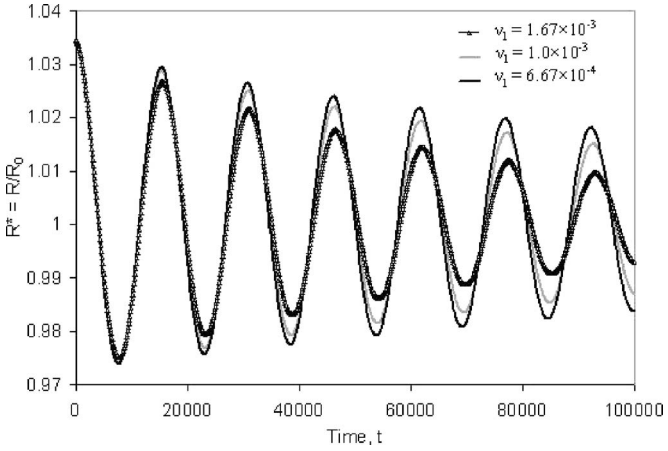

FIG. 6. Oscillation of an initially ellipsoidal drop at different viscosities; $\rho_l/\rho_g=1,000$, $\mu_l/\mu_g=40$, and $\sigma=0.0003$.

($R_{\max}$) of 22 and 24, respectively. The bottom boundary is the axis of symmetry and the drop center is located at the middle of the axis of symmetry. The initial minimum radius is along the axisymmetric boundary of the domain. Periodic boundary conditions are employed at the left and right boundaries. The top boundary is closed and a slip bounce-back condition is employed. The domain size is 100×50. In the figure, the position of the interface along the major radius is shown. The interface location is nondimensionalized by $R_0=(R_{\max}^2R_{\min})^{1/3}$. In all cases, $\rho_l/\rho_g=1000$, $\mu_l/\mu_g=40$, $\sigma=0.0001$, and $D=5$. The drop relaxation parameters are $\tau_l=0.505$, 0.503, and 0.502, which correspond to nondimensional drop kinematic viscosities of $\nu_l=1.6667\times10^{-3}$, 1.0×10^{-3}, and 6.6667×10^{-4}, respectively. However, as τ_l approaches 0.5, i.e., when ν_l is small, LB schemes become numerically unstable due to the growth of spurious currents [5–7,13,15–17]. The same trend is observed in our computation. The minimum value of τ_l possible is problem-dependent. In this particular computation, the minimum τ_l at which drop oscillation computations give stable solution is 0.502.

Comparing these cases in Fig. 5, the amplitude of the oscillation decays slower as the viscosity is reduced, as expected. The computed time periods of oscillation are 27 106, 26 953, and 26 853 when the viscosities are 1.6667×10^{-3}, 1.0×10^{-3}, and 6.6667×10^{-4}, respectively. The corresponding analytical time period of oscillation T_{anal} is 25 072. Thus, the maximum error is about 8%. As the viscosity is lowered, the computed solution approaches the analytical solution in Eq. (78), which is formulated for inviscid fluid.

Figure 6 shows oscillations when the surface tension is increased to 0.0003. As expected the oscillation time periods decrease with increase in σ. For example, when $\nu_l=6.6667\times10^{-4}$, the computed time period $T_{LBM}=15\,451$, which is lower than $T_{LBM}=26\,853$, observed at $\sigma=0.0001$ for the same viscosity. The computed time periods are within 7.4% of the analytical time period $T_{anal}=14\,434$. To confirm the trend with change in surface tension, σ is further increased to 0.0005. The oscillations are shown in Fig. 7. T_{LBM} is found to be 11 921 at $\upsilon_l=6.6667\times10^{-4}$, which again is lower than T_{LBM} computed at $\sigma=0.0001$ and 0.0003. The

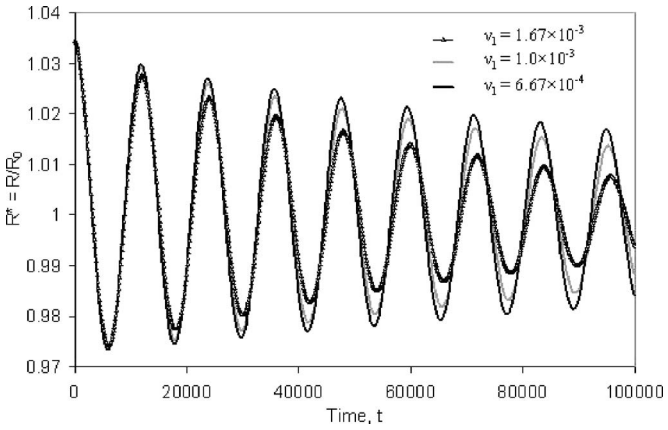

FIG. 7. Oscillation of an infinitely long liquid cylinder initially with an elliptical cross section, at different viscosities; $\rho_l/\rho_g=1000$, $\mu_l/\mu_g=40$, and $\sigma=0.0005$.

computed time periods are within 6.9% of the analytical time period $T_{anal}=11\,180$. Therefore computations are able to reproduce the surface tension influence on oscillation given by the analytical expression.

Next we consider a more complex dynamical case of a spherical liquid drop impinging on a wet wall. To our best knowledge, there is no prior work available demonstrating *spherical* drop impingement on a wet wall employing LBM. In the study of impingement on wet walls, the major dimensionless parameters of interest are the impact Weber number We, the Reynolds number Re, and the nondimensional wall film thickness H^*. They are defined as

$$\mathrm{We}=\frac{\rho_l D_0 U_0^2}{\sigma}, \tag{79}$$

$$\mathrm{Re}=\frac{\rho_l U_0 D_0}{\mu_l}, \tag{80}$$

$$H^*=\frac{H}{D_0}, \tag{81}$$

where ρ_l is the density of the drop, D_0 is the diameter of the drop, H is the wall liquid layer thickness, U_0 is the impact velocity, σ is the surface tension, and μ_l the dynamic viscosity. The subscript l is for the liquid. The impingement outcomes are splash and deposition. At low Re, the impinged drop deposits on the surface, whereas at high Re, a thin liquid jet is ejected at the moment of impact from the narrow region where the drop surface contacts the wall liquid layer. This liquid jet grows with time, forming a crownlike liquid sheet that propagates radially outward from the center of the impact. The crown is unstable and may break up, forming secondary droplets. In Ref. [17] impingement results were reported for a liquid *cylinder* impacting at We=8000 and Re=500. The other parameters were $H^*=0.15$, $\rho_l/\rho_g=1000$, and $\mu_l/\mu_g=40$. In this work, we employ that same set of parameters. However, with the axisymmetric model we simulate impingement of a spherical drop instead of the planar 2D liquid cylinder. The interface thickness parameter D is 5. The snapshots of the impingement process are shown in Fig. 8. The simulation domain is 600×400. The time is nondimensionalized as $t^*=U_0t/D_0$. In the figure, the evolution of the density contour $\rho_m=(\rho_l+\rho_g)/2$ is shown up to $t^*=2.85$. At $t^*=0$ the drop comes in contact with the wall liquid layer. After the drop impinges, a radial jet is observed along the outer periphery of the drop layer contact surface (see $t^*=0.3$ and $t^*=1.15$). The radial jet grows with time, forming a corona ($t^*=2.5$). The corona propagates outward, its thickness decreases, and height increases before it breaks up ($t^*=2.85$), detaching a ligament at the tip. In potential flow models, in the early stages of impact, the temporal evolution of the corona tip distance from the impingement axis is observed to follow a power-law spreading behavior [25,26]. In Fig. 9, the distance of the tip of the corona from the impingement axis is plotted as it evolves with time. The tip distance r is nondimensionalized by the initial drop diameter as $R^*=r/D_0$. In the computation, R^* is observed to follow $t^{*0.5}$ scaling for up to $t^*=2.5$, after which the corona breaks up. This trend could not be reproduced beyond $t^*>0.2$ by the 2D planar computations of liquid cylinder impingement reported by Lee and Lin.

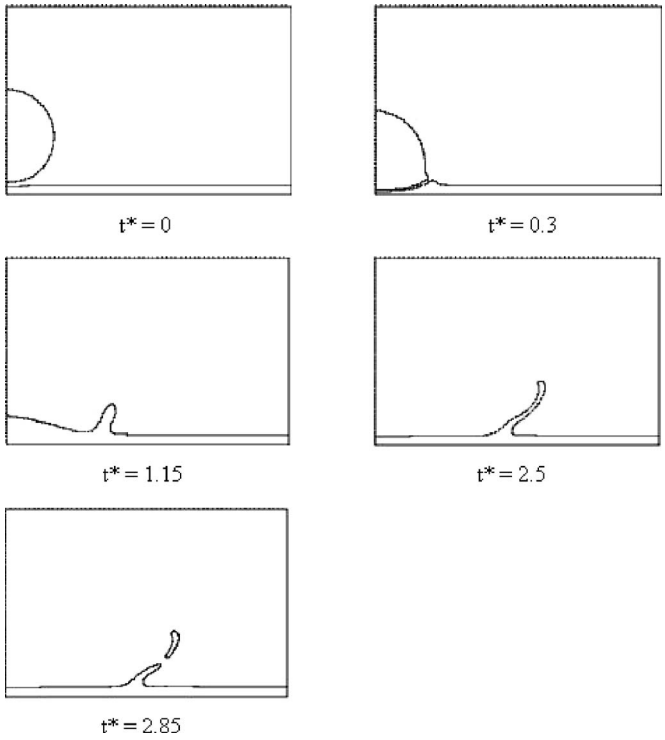

FIG. 8. Snapshots of drop impingement on wet wall; We=8000, Re=500, $H^*=0.15$, $\rho_l/\rho_g=1000$, and $\mu_l/\mu_g=40$.

V. SUMMARY AND CONCLUSIONS

In this paper, a high-density-ratio lattice Boltzmann model developed by Lee and Lin is adapted for axisymmetric computations and the use of a multiple-relaxation-time collision model. With this model, axisymmetric simulations can be performed with liquid-to-gas density ratios as high as 1000. To recover the axisymmetric mass and momentum conserva-

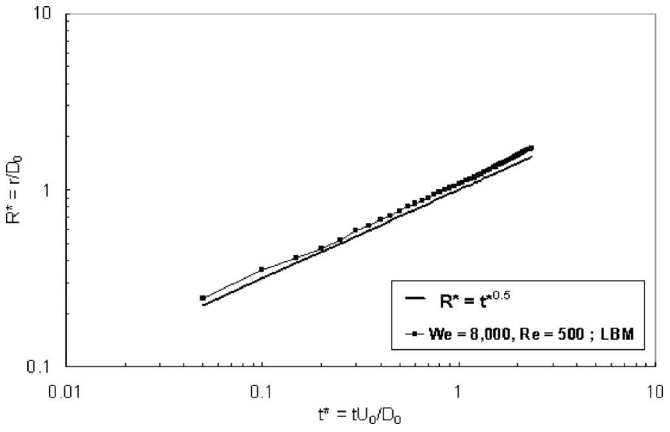

FIG. 9. Time evolution of the radial distance of the tip of the corona from the impingement axis; We=8000, Re=500, $H^*=0.15$, $\rho_l/\rho_g=1000$, and $\mu_l/\mu_g=40$.

tion equations, source terms are added in the evolution equations for the distribution functions that give density and pressure. These include source terms to recover mass, momentum, and viscous and capillary tensors in the axisymmetric framework. The pressure function, which varies smoothly across the interface, is modified to include the influence of interfacial curvature in the azimuthal direction. In applying the MRT model, the collision terms are treated explicitly whereas the source terms are treated semi-implicitly. The three-step solution procedure proposed by Lee and Lin, involving prestreaming collision, streaming, and poststreaming collision, is employed for the solution of the discrete equations. The axisymmetric source terms in the density and pressure equations due to capillary tensor are treated as directional derivatives and discretized in the respective lattice-velocity directions, while the remaining source terms are treated as partial derivatives. The model is evaluated for accuracy by solving three two-phase flow test problems. In the problems, the density ratio and viscosity ratios are maintained at 1000 and 40, respectively, which approximate the property of water in air. These values were not attainable with the earlier axisymmetric multiphase MRT model of Premnath and Abraham. Laplace's law is verified for a spherical liquid drop to within 3% accuracy. In the computations of drop oscillations, the computed periods of oscillation are within 8% of the analytical solution. The model is then employed to simulate drop impingement on a wet wall. Computed solutions reproduced the power-law growth of the corona up to the point when the corona breaks up.

APPENDIX A

Integrating Eq. (34) along the characteristics we obtain

$$f_\alpha(x+e_\alpha\delta_t,t+\delta_t)-f_\alpha(x,t) = -\frac{1}{\tau}(f_\alpha-f_\alpha^{eq})+\frac{(e_{\alpha i}-u_i)F_i^{tp}}{c_s^2}\Gamma_\alpha(\mathbf{u})\delta_t+(S_{f\alpha}^{a_0}+S_{f\alpha}^{a_1})\delta_t, \tag{A1}$$

where

$$F_i^{tp}=\partial_i\rho c_s^2-\rho\partial_i\left(\frac{\partial E_f}{\partial\rho}-\kappa\partial_j^2\rho\right). \tag{A2}$$

Introducing the Chapman-Enskog expansion,

$$f_\alpha(x+e_\alpha\delta_t,t+\delta_t)=\sum_{n=0}^{\infty}D_{t_n}f_\alpha(x,t), \tag{A3}$$

$$D_{t_n}=\partial_{t_n}+e_{\alpha k}\partial_k, \tag{A4}$$

$$f_\alpha=\sum_{n=0}^{\infty}\varepsilon^n f_\alpha^{(n)}, \tag{A5}$$

$$\partial_t=\sum_{n=0}^{\infty}\varepsilon^n\partial_{t_n}, \tag{A6}$$

where

$$\varepsilon=\delta_t, \tag{A7}$$

$$\sum_\alpha\begin{pmatrix}1\\e_{\alpha i}\end{pmatrix}f_\alpha^{(0)}=\begin{pmatrix}\rho\\\rho u_i\end{pmatrix}, \tag{A8}$$

$$\sum_\alpha\begin{pmatrix}1\\e_{\alpha i}\end{pmatrix}f_\alpha^{(n)}=\begin{pmatrix}0\\0\end{pmatrix},\quad n\geqslant 1, \tag{A9}$$

the following equations are obtained up to second order of the parameter ε:

$$O(\varepsilon^0):\ f_\alpha^{(0)}=f_\alpha^{eq}, \tag{A10}$$

$$O(\varepsilon^1):\ D_{t_0}f_\alpha^{(0)}=-\frac{1}{\tau}f_\alpha^{(1)}+\frac{(e_{\alpha i}-u_i)F_i^{tp}}{c_s^2}\Gamma_\alpha(\mathbf{u})+S_{f\alpha}^{a_0}+S_{f\alpha}^{a_1}, \tag{A11}$$

$$O(\varepsilon^2):\ \partial_{t_1}f_\alpha^{(0)}+\left(1-\frac{1}{2\tau}\right)D_{t_0}f_\alpha^{(1)}=-\frac{1}{\tau}f_\alpha^{(2)}. \tag{A12}$$

Note that

$$\sum_\alpha S_{f\alpha}^{a_0}=\sum_\alpha -w_\alpha\frac{\rho u_y}{y}=-\frac{\rho u_y}{y}, \tag{A13}$$

$$\sum_\alpha S_{f\alpha}^{a_1}=\sum_\alpha\frac{(e_{\alpha i}-u_i)F_{fi}^{ax}}{c_s^2}\Gamma_\alpha(\mathbf{u})=0. \tag{A14}$$

Therefore, $\Sigma_\alpha(\cdot)$ is employed in Eqs. (A11) and (A12), and the resulting equations are summed to obtain the axisymmetric mass conservation [Eq. (27)] up to $O(\varepsilon^2)$ accuracy. Next, we note that the first kinetic moment of the axisymmetric source terms are as follows:

$$\sum_{\alpha} e_{\alpha i} S_{f\alpha}^{a_0} = \sum_{\alpha} -e_{\alpha i} w_{\alpha} \frac{\rho u_y}{y} = 0, \tag{A15}$$

$$\sum_{\alpha} e_{\alpha i} S_{f\alpha}^{a_1} = \sum_{\alpha} e_{\alpha i} \frac{(e_{\alpha k} - u_k) F_{fk}^{ax}}{c_s^2} \Gamma_{\alpha}(\mathbf{u}) = F_{fi}^{ax}. \tag{A16}$$

Hence, applying $\Sigma_{\alpha} e_{\alpha i}(\cdot)$ to Eqs. (A11) and (A12) and summing the resulting equations, we obtain the axisymmetric momentum conservation equation [Eqs. (28) and (29)] up to $O(\varepsilon^2)$ accuracy.

APPENDIX B

We integrate Eq. (51) along the characteristics to obtain

$$\begin{aligned} g_{\alpha}(x + e_{\alpha}\delta_t, t + \delta_t) - g_{\alpha}(x,t) &= -\frac{1}{\tau}(g_{\alpha} - g_{\alpha}^{eq}) + \frac{(e_{\alpha i} - u_i)\partial_i(\rho c_s^2 - p)}{c_s^2}[\Gamma_{\alpha}(\mathbf{u}) - \Gamma_{\alpha}(0)]\delta_t \\ &+ \frac{(e_{\alpha i} - u_i)[\kappa \partial_i(\partial_k \rho \partial_k \rho) - \kappa \partial_j(\partial_i \rho \partial_j \rho)]}{c_s^2} \Gamma_{\alpha}(\mathbf{u})\delta_t \\ &+ (S_{g\alpha}^{a_0} + S_{g\alpha}^{a_1})\delta_t. \end{aligned} \tag{B1}$$

Then, Chapman-Enskog expansion is employed as in Eqs. (A1)–(A7) by replacing f with g. Recognizing that

$$\sum_{\alpha} \begin{pmatrix} 1 \\ e_{\alpha i} \end{pmatrix} g_{\alpha}^{(0)} = \begin{pmatrix} \dfrac{p}{c_s^2} \\ \rho u_i \end{pmatrix} \tag{B2}$$

and

$$\sum_{\alpha} \begin{pmatrix} 1 \\ e_{\alpha i} \end{pmatrix} g_{\alpha}^{(n)} = \begin{pmatrix} 0 \\ 0 \end{pmatrix}, \quad n \geqslant 1, \tag{B3}$$

we obtain the following in orders of ε:

$$O(\varepsilon^0): \; g_{\alpha}^{(0)} = g_{\alpha}^{eq}, \tag{B4}$$

$$\begin{aligned} O(\varepsilon^1): \; D_{t_0} g_{\alpha}^{(0)} &= -\frac{1}{\tau} g_{\alpha}^{(1)} \\ &+ \frac{(e_{\alpha i} - u_i)[\kappa \partial_i(\partial_k \rho \partial_k \rho) - \kappa \partial_j(\partial_i \rho \partial_j \rho)]}{c_s^2} \Gamma_{\alpha}(\mathbf{u}) \\ &+ S_{g\alpha}^{a_0} + S_{g\alpha}^{a_1}, \end{aligned} \tag{B5}$$

and

$$O(\varepsilon^2): \; \partial_{t_1} g_{\alpha}^{(0)} + \left(1 - \frac{1}{2\tau}\right) D_{t_0} g_{\alpha}^{(1)} = -\frac{1}{\tau} g_{\alpha}^{(2)}. \tag{B6}$$

The zeroth- and the first-order kinetic moment of the axisymmetric source terms are as follows:

$$\sum_{\alpha} S_{g\alpha}^{a_0} = \sum_{\alpha} -w_{\alpha} \frac{\rho u_y}{y} = -\frac{\rho u_y}{y}, \tag{B7}$$

$$\sum_{\alpha} e_{\alpha i} S_{g\alpha}^{a_1} = \sum_{\alpha} e_{\alpha i} \frac{(e_{\alpha k} - u_k) F_{gk}^{ax}}{c_s^2} \Gamma_{\alpha}(\mathbf{u}) = F_{gi}^{ax}, \tag{B8}$$

$$\sum_{\alpha} e_{\alpha i} S_{g\alpha}^{a_0} = \sum_{\alpha} -e_{\alpha i} w_{\alpha} \frac{\rho u_y}{y} = 0, \tag{B9}$$

$$\sum_{\alpha} e_{\alpha i} S_{g\alpha}^{a_1} = \sum_{\alpha} e_{\alpha i} \frac{(e_{\alpha k} - u_k) F_{gk}^{ax}}{c_s^2} \Gamma_{\alpha}(\mathbf{u}) = F_{gi}^{ax}. \tag{B10}$$

Therefore, applying $\Sigma_{\alpha}(\cdot)$ to Eqs. (B5) and (B6) and summing the resulting equations, we obtain the axisymmetric zero-velocity divergence equation [Eq. (46)] up to $O(\varepsilon^2)$ accuracy. By applying $\Sigma_{\alpha} e_{\alpha i}(\cdot)$ to Eqs. (B5) and (B6) and summing the resulting equations, we obtain the axisymmetric momentum conservation equation [Eqs. (47) and (48)] up to $O(\varepsilon^2)$ accuracy.

APPENDIX C

We couple Eq. (A11) and Eq. (A12) to obtain

$$\partial_t \rho + \partial_k(\rho u_k) = -\frac{\rho u_y}{y} - \left(1 - \frac{1}{2\tau}\right) \delta_t \partial_k \left(\sum_{\alpha} f_{\alpha}^{(1)} e_{\alpha k} \right). \tag{C1}$$

Next, using Eq. (A11) $f_{\alpha}^{(1)}$ is expressed in terms of $f_{\alpha}^{(0)}$, which gives

$$\begin{aligned} \sum_{\alpha} f_{\alpha}^{(1)} e_{\alpha i} &= -\tau \left[\partial_{t_0} \left(\sum_{\alpha} f_{\alpha}^{(0)} e_{\alpha i} \right) + \partial_k \left(\sum_{\alpha} e_{\alpha i} e_{\alpha k} f_{\alpha}^{(0)} \right) \right] \\ &+ \tau \sum_{\alpha} e_{\alpha i} \left[\frac{(e_{\alpha i} - u_i) F_i^{ip}}{c_s^2} \Gamma_{\alpha}(u) + S_{f\alpha}^{a_0} + S_{f\alpha}^{a_1} \right]. \end{aligned} \tag{C2}$$

This again can be expressed by replacing the first- and second-order moments of $f_{\alpha}^{(0)}$ in terms of density and velocity as [10]

$$\begin{aligned} \sum_{\alpha} f_{\alpha}^{(1)} e_{\alpha i} &= -\tau [\partial_{t_0}(\rho u_i) + \partial_i(\rho c_s^2) + \partial_j(\rho u_i u_j)] \\ &+ \tau \left[\partial_i(\rho c_s^2) - \rho \partial_i \left(\frac{\partial E_f}{\partial \rho} - \kappa \partial_k \partial_k \rho \right) + F_{fi}^{ax} \right]. \end{aligned} \tag{C3}$$

Next, in Eq. (C3), $\partial_{t_0}(\rho u_i)$ is replaced by a first-order momentum equation, as given by

$$\partial_{t_0}(\rho u_i) = -\partial_i p - \partial_j(\rho u_i u_j) + \kappa[\partial_i(\partial_k \rho \partial_k \rho) - \partial_j(\partial_i \rho \partial_j \rho)] + F_{gi}^{ax}. \tag{C4}$$

Then the relation $\rho \partial_i(\partial E_f / \partial \rho) = \partial_i P$ is used. The resulting expression for $\Sigma_{\alpha} f_{\alpha}^{(1)} e_{\alpha i}$ is then substituted in Eq. (C1) to get Eq. (55).

[1] X. Shan and H. Chen, Phys. Rev. E **47**, 1815 (1993).
[2] S. Chen and G. D. Doolen, Annu. Rev. Fluid Mech. **30**, 329 (1998).
[3] R. Benzi, S. Succi, and M. Vergassola, Phys. Rep. **222**, 145 (1992).
[4] R. Nourgaliev, T. Dinh, T. Theofanous, and D. Joseph, Int. J. Multiphase Flow **29**, 117 (2003).
[5] X. He, S. Chen, and R. Zhang, J. Comput. Phys. **152**, 642 (1999).
[6] K. N. Premnath and J. Abraham, Phys. Fluids **17**, 122105 (2005).
[7] M. E. McCracken and J. Abraham, Int. J. Mod. Phys. C **16**, 1671 (2005).
[8] L. Kadanoff, Phys. Today **39**, 7 (1986).
[9] S. Wolfram, J. Stat. Phys. **45**, 471 (1986).
[10] X. He and L. S. Luo, Phys. Rev. E **56**, 6811 (1997).
[11] K. N. Premnath and J. Abraham, Phys. Rev. E **71**, 056706 (2005).
[12] S. Teng, Y. Chen, and H. Ohashi, Int. J. Heat Fluid Flow **21**, 112 (2000).
[13] K. Sankaranarayanan, X. Shan, I. G. Kevrekidis, and S. Sundaresan, J. Fluid Mech. **452**, 61 (2002).
[14] P. Bhatnagar, E. Gross, and M. Krook, Phys. Rev. **94**, 511 (1954).
[15] T. Inamuro, T. Ogata, S. Tajima, and N. Konishi, J. Comput. Phys. **198**, 628 (2004).
[16] T. Lee and C. L. Lin, Phys. Rev. E **67**, 056703 (2003).
[17] T. Lee and C. L. Lin, J. Comput. Phys. **206**, 16 (2005).
[18] H. W. Zheng, C. Shu, and Y. T. Chew, J. Comput. Phys. **218**, 353 (2006).
[19] A. Lamura and S. Succi, Int. J. Mod. Phys. B **17**, 145 (2003).
[20] D. D'Humieres, Prog. Aeronaut. Astronaut. **159**, 450 (1992).
[21] P. Lallemand and L. S. Luo, Phys. Rev. E **61**, 6546 (2000).
[22] M. E. McCracken and J. Abraham, Phys. Rev. E **71**, 036701 (2005).
[23] I. Halliday, L. A. Hammond, C. M. Care, K. Good, and A. Stevens, Phys. Rev. E **64**, 011208 (2001).
[24] H. Lamb, *Hydrodynamics* (Cambridge University Press, Cambridge, England, 1932).
[25] A. L. Yarin and D. A. Weiss, J. Fluid Mech. **283**, 141 (1995).
[26] C. Josserand and S. Zaleski, Phys. Fluids **15**, 1650 (2003).